


Magnon-photon strong coupling for tunable microwave circulatorsNa Zhu , Xu Han, Chang-Ling Zou,^{*} Mingrui Xu, and Hong X. Tang[†]*Department of Electrical Engineering, Yale University, New Haven, Connecticut 06520, USA*

(Received 8 December 2019; accepted 23 March 2020; published 28 April 2020)

We present a generic theoretical framework to describe nonreciprocal microwave circulation in a multimode cavity magnonic system and assess the optimal performance of practical circulator devices. We show that high isolation (> 56 dB), extremely low insertion loss (< 0.05 dB), and flexible bandwidth control can be potentially realized in high-quality-factor superconducting cavity based magnonic platforms. These circulation characteristics are analyzed with materials of different spin densities. For high-spin-density materials such as yttrium iron garnet, the strong-coupling operation regime can be harnessed to obtain a broader circulation bandwidth. We also provide practical design principles for a highly integratable low-spin-density material (vanadium tetracyanoethylene) for narrow-band circulator operation, which could benefit noise-sensitive quantum microwave measurements. This theory can be extended to other coupled systems and provide design guidelines for achieving tunable microwave nonreciprocity for both classical and quantum applications.

DOI: [10.1103/PhysRevA.101.043842](https://doi.org/10.1103/PhysRevA.101.043842)**I. INTRODUCTION**

Nonreciprocal microwave devices are ubiquitous and important in classical and quantum information processing, as they protect delicate measurements from reflected signals [1]. The nonreciprocal effect arises from broken time-reversal symmetry, traditionally realized with ferrite materials [2–4]. Recently, a variety of avenues have been reported to realize nonreciprocity without the use of magnetic materials, including optomechanical coupling [5,6], reservoir engineering [7,8], nonlinear effect [9,10], and temporal modulation [11]. Those approaches, albeit being nonmagnetic, typically require strict phase matching condition and have limited tunability [5–7,9,10], with added complexity in experimental implementations. Nowadays, due to the high demand in sensitive microwave signal detections, especially at the single-photon level for superconducting quantum circuits, low-loss, tunable, and compact electromagnetic circulator devices are of great interest [1].

Cavity magnonic systems have attracted significant attention recently [12–23] due to the strong interaction between magnon excitations and microwave photons. Previous studies have demonstrated magnon-photon strong coupling in various resonant microwave systems, such as copper three-dimensional (3D) cavities [14–18] and coplanar microwave circuits [19,20,24]. However, those cavity magnonic systems are in the conventional coherent coupling configuration, where magnons are coupled with a single microwave mode without any nonreciprocal effect. Only a few recent works have investigated nonreciprocal coherent or dissipative magnon-photon coupling in two-port systems to demonstrate isolator devices [25,26]. The study of the three-port nonreciprocal magnonic platform is highly motivated because of

its applications in sensitive cryogenic microwave reflection measurements [27,28].

In this work, we present a generic theoretical model for nonreciprocal multimode cavity magnonic systems. We show that by harnessing the selective coupling between the magnon mode and microwave modes with different chiralities, as well as the interference effect between different paths in a three-port system, nonreciprocal microwave circulation with high isolation, low insertion loss, and flexible controllability can be achieved. For device implementation, we propose a practical design based on a high-quality factor (Q) superconducting ring resonator which is coupled with a high- Q magnon mode in a low-Gilbert-damping magnetic media [12,29] under a bias magnetic field. Two exemplary material platforms are discussed: (1) yttrium iron garnet (YIG), a high-spin-density material that can work in the strong-coupling regime to obtain broader circulation bandwidth [30], and (2) vanadium tetracyanoethylene ($V[TCNE]_2$), a highly integratable low-spin-density material for narrow-bandwidth operation [31]. Unlike commercial circulators designed for octave broadband operations, this work exploits cavity enhanced circulation effect and trades the circulation bandwidth for high isolation and low insertion loss, which are the most desirable performance parameters for delicate single-photon-level quantum measurements.

II. THEORETICAL MODEL**A. Coupled-mode theory**

A schematic of the circulator is shown in Fig. 1(a), where a three-port superconducting ring resonator simultaneously supports two degenerate counter-rotating microwave modes. This ring resonator is aligned with a ferrimagnetic disk of similar dimension for optimal mode overlap. Under a static out-of-plane magnetic bias field, the ferrimagnetic disk supports a uniform magnon mode with the resonant frequency linearly proportional to the external field [32], $\omega_m \approx \gamma |\vec{B}_0|$,

^{*}Present address: Department of Optics, University of Science and Technology of China, Hefei 230026, China.

[†]hong.tang@yale.edu

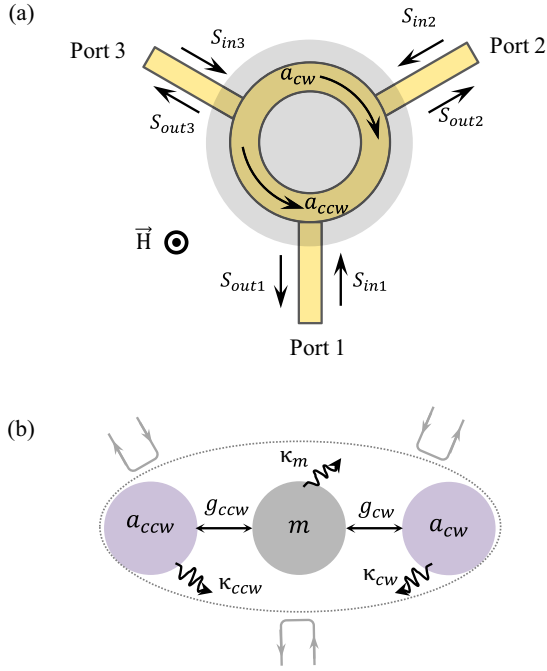


FIG. 1. (a) Schematic diagram of the device. The superconducting ring resonator supports both counterclockwise (ccw; a_{ccw}) and clockwise (cw; a_{cw}) rotating microwave modes. A ferrimagnetic disk (gray color) with similar dimension is placed on top of the superconducting ring and biased perpendicularly. There are three straight waveguides with threefold geometrical symmetry inductively coupled with the ring resonator. (b) The schematic shows the magnon-photon coupling, where the microwave mode a_{ccw} is coupled with the magnon mode m with the coupling strength g_{ccw} , while mode a_{cw} is coupled with magnon mode via a different coupling strength g_{cw} . κ_{ccw} , κ_{cw} , and κ_m are the total dissipation rates for mode a_{ccw} , a_{cw} , and m , respectively.

where $\gamma = 2.8$ MHz/Oe is the gyromagnetic ratio. The system Hamiltonian can be written as

$$H/\hbar = \omega_{ccw} a_{ccw}^\dagger a_{ccw} + \omega_{cw} a_{cw}^\dagger a_{cw} + \omega_m m^\dagger m + H_{int}/\hbar. \quad (1)$$

Here, a_{ccw} (a_{ccw}^\dagger), a_{cw} (a_{cw}^\dagger), m (m^\dagger) are the annihilation (creation) operators for the counterclockwise (ccw) and the clockwise (cw) microwave mode, and the magnon mode, respectively, with their resonant frequencies denoted as ω_{ccw} , ω_{cw} , and ω_m . Since the ccw and the cw modes are orthogonal, we only need to consider their linear coupling with the magnon mode in our system. So the interaction Hamiltonian is

$$H_{int}/\hbar = -g_{ccw}(a_{ccw} + a_{ccw}^\dagger)(m + m^\dagger) - g_{cw}(a_{cw} + a_{cw}^\dagger)(m + m^\dagger), \quad (2)$$

where g_{ccw} and g_{cw} are the coupling strengths between the respective microwave mode and magnon mode [26,33,34].

Under the rotating wave approximation, the Heisenberg-Langevin equation can be written as

$$\dot{\mathbf{a}} = \mathbf{M}_1 \mathbf{a} + \mathbf{K} \mathbf{s}_{in}, \quad (3)$$

with the input-output relation

$$\mathbf{s}_{out} = \mathbf{C} \mathbf{s}_{in} + \mathbf{M}_2 \mathbf{a}. \quad (4)$$

Here $\mathbf{a} = \{a_{ccw}, a_{cw}, m\}^T$ is the vector of the cavity field. $\mathbf{s}_{in} = \{s_{in1}, s_{in2}, s_{in3}\}^T$ and $\mathbf{s}_{out} = \{s_{out1}, s_{out2}, s_{out3}\}^T$ are the input and the output fields at the three ports. Matrix \mathbf{M}_1 (3×3) is given as

$$\mathbf{M}_1 = \begin{pmatrix} -i\omega_{ccw} - \frac{\kappa_{ccw}}{2} & 0 & ig_{ccw} \\ 0 & -i\omega_{cw} - \frac{\kappa_{cw}}{2} & ig_{cw} \\ ig_{ccw} & ig_{cw} & -i\omega_m - \frac{\kappa_m}{2} \end{pmatrix}, \quad (5)$$

in which κ_{ccw} , κ_{cw} , and κ_m are the total dissipation rates for the microwave and magnon modes, respectively. \mathbf{K} and \mathbf{M}_2 are the (3×3) matrices describing the coupling of three incoming and outgoing waves with two resonant modes. Based on the relation among \mathbf{K} , \mathbf{C} , and \mathbf{M}_2 (see Appendix), the matrix \mathbf{K} (3×3) satisfies the energy conservation relation $\mathbf{K}\mathbf{K}^\dagger = \mathbf{\Gamma}_e$, and can be in general written as

$$\mathbf{K} = -\mathbf{M}_2^\dagger \mathbf{C} = \begin{pmatrix} \sqrt{\kappa_{ccw,e1}} & \sqrt{\kappa_{ccw,e2}} e^{i\alpha} & \sqrt{\kappa_{ccw,e3}} e^{i\eta} \\ \sqrt{\kappa_{cw,e1}} e^{i\beta_1} & \sqrt{\kappa_{cw,e2}} e^{i\beta_2} & \sqrt{\kappa_{cw,e3}} e^{i\beta_3} \\ 0 & 0 & 0 \end{pmatrix}. \quad (6)$$

Here $\alpha(\eta)$ is the relative phase between the excitation port 2(3) and port 1 for mode a_{ccw} . β_1 describes the phase difference between cw and ccw modes at port 1, and $(\beta_{2(3)} - \beta_1)$ denotes the relative phase difference for the cw mode between port 2(3) and 1. $\kappa_{ccw,e1(2,3)}$ and $\kappa_{cw,e1(2,3)}$ represent the external coupling rates of the two microwave modes to the three input and output ports, respectively.

\mathbf{C} is the (3×3) matrix describing direct coupling of incoming and outgoing waves. Due to energy conservation, \mathbf{C} must be unitary $\mathbf{C}^\dagger \mathbf{C} = \mathbf{I}$. But the specific expression for \mathbf{C} depends on the physical implementation of the excitation ports. For example, in the case of a waveguide end-coupling scheme with negligible crosstalk between ports, $\mathbf{C} = \mathbf{I}$ for open-ended (capacitive) coupling [35,36]; and $\mathbf{C} = -\mathbf{I}$ for short-ended (inductive) coupling [35,37–39]. In this paper, we assume that the waveguides and the ring are inductively coupled with no dissipative coupling across different ports, namely,

$$\mathbf{C} = \begin{pmatrix} -1 & 0 & 0 \\ 0 & -1 & 0 \\ 0 & 0 & -1 \end{pmatrix}. \quad (7)$$

With the expressions of matrices in Eqs. (3) and (4), the equation of motion can be solved in frequency domain to obtain the scattering matrix (defined by $\mathbf{s}_{out}[\omega] = \mathbf{S}[\omega] \mathbf{s}_{in}[\omega]$)

$$\mathbf{S}[\omega] = \mathbf{C} + \mathbf{M}_2 [-i\omega \mathbf{I} - \mathbf{M}_1]^{-1} \mathbf{K}. \quad (8)$$

B. Circulation under threefold symmetry

Based on the generic coupled-mode theory described above, we now focus our discussion on the system circulation with threefold geometrical rotational symmetry. Under this condition, the microwave modes a_{ccw} and a_{cw} are degenerate and have external coupling rates to each of the three waveguides with the value $\kappa_e/3$. The total dissipation rate $\kappa_{ccw} = \kappa_{cw} = \kappa_e + \kappa_i$, where κ_i and κ_e are the microwave intrinsic dissipation and total external coupling rates, respectively.

At the same time, we have the relative excitation phase difference between port 2(3) and 1 as $\alpha = -\eta = -2n\pi/3$, where n is the integer representing the mode number. Here, we focus on the two degenerate fundamental circulation microwave modes ($n = 1$), for which we have $\omega_{ccw} = \omega_{cw}$ and $\alpha = -\eta = -2\pi/3$. Such phase difference is determined by the threefold rotational symmetry, because the fundamental mode is formed when the wavelength equals the ring perimeter with the azimuthal number to be 1, leading to a 2π phase shift along the ring [2,4]. The relative phase difference between two ports under threefold rotational symmetry will be $\pm 2\pi/3$, depending on the mode propagating directions. Since these two modes are orthogonal to each other, it can be shown that the relative excitation phase β_1 between a_{ccw} and a_{cw} does not contribute to the final expression of the scattering matrix, and we can set that to be 0 for simplicity.

Due to the selective coupling rule, the magnon mode would only couple with microwave mode with the same chirality. Therefore, for our two circular microwave modes, only $g_{ccw} =$

g is significant and $g_{cw} \approx 0$. It is worth pointing out that a different eigenmode basis can be chosen for the two degenerate microwave modes by applying a unitary rotation

$$U(\theta) = \begin{pmatrix} \cos\theta & -\sin\theta & 0 \\ \sin\theta & \cos\theta & 0 \\ 0 & 0 & 1 \end{pmatrix}$$

. Then the new \mathbf{M}_1 matrix will become the general form in Eq. (5) with $g_{ccw} = g \sin\theta$ and $g_{cw} = -g \cos\theta$. This rotation of the basis, nevertheless, will not change the physical results of our analysis.

Under the threefold geometrical symmetry, the coupling matrix \mathbf{K} is given by

$$\mathbf{K} = \sqrt{\frac{\kappa_e}{3}} \begin{pmatrix} 1 & e^{-i(2\pi/3)} & e^{i(2\pi/3)} \\ 1 & e^{i(2\pi/3)} & e^{-i(2\pi/3)} \\ 0 & 0 & 0 \end{pmatrix}. \quad (9)$$

Finally, using Eq. (8), we can obtain the scattering matrix elements

$$S_{11} = S_{22} = S_{33} = -1 + \frac{\kappa_e}{3[\kappa_{cw}/2 - i(\omega - \omega_{cw})]} + \frac{\kappa_e[\kappa_m/2 - i(\omega - \omega_m)]}{3\{g^2 + [\kappa_m/2 - i(\omega - \omega_m)][\kappa_{ccw}/2 - i(\omega - \omega_{ccw})]\}}, \quad (10)$$

$$S_{12} = S_{23} = S_{31} = \frac{e^{i2\pi/3}\kappa_e}{3[\kappa_{cw}/2 - i(\omega - \omega_{cw})]} + \frac{e^{-i2\pi/3}\kappa_e[\kappa_m/2 - i(\omega - \omega_m)]}{3\{g^2 + [\kappa_m/2 - i(\omega - \omega_m)][\kappa_{ccw}/2 - i(\omega - \omega_{ccw})]\}}, \quad (11)$$

$$S_{21} = S_{13} = S_{32} = \frac{e^{-i2\pi/3}\kappa_e}{3[\kappa_{cw}/2 - i(\omega - \omega_{cw})]} + \frac{e^{i2\pi/3}\kappa_e[\kappa_m/2 - i(\omega - \omega_m)]}{3\{g^2 + [\kappa_m/2 - i(\omega - \omega_m)][\kappa_{ccw}/2 - i(\omega - \omega_{ccw})]\}}. \quad (12)$$

We see that the scattering matrix satisfies relations $S_{11} = S_{22} = S_{33}$, $S_{12} = S_{23} = S_{31}$, and $S_{21} = S_{13} = S_{32}$, as expected from the rotational symmetry. Without the threefold symmetry, for example, if three waveguides are designed to have different dimensions, the microwave external coupling rates for three ports are very different, and the reflection coefficients could be in general different, $S_{11} \neq S_{22} \neq S_{33}$. Such degeneracy will also be broken for other transmission parameters. Hence, if the microwave circuit is designed to be nonsymmetric, the system circulation performance is only optimized for one kind of connection configuration under certain magnetic bias condition.

Next, as we can see from Eqs. (10)–(12), although the microwave ccw and cw modes are degenerate due to the structural symmetry, selective coupling between the magnon mode and the two rotational microwave modes gives rise to a nonreciprocal scattering matrix. If there is no magnon-photon coupling ($g = 0$), S_{12} and S_{21} do not have the amplitude nonreciprocity. In the situation when ($g \neq 0$), the signal circulation starts to occur due to magnon-coupling-induced interference; the isolation ratio between the scattering matrix parameters S_{12} and S_{21} depends on both g and the magnon resonance detuning ($\omega_{ccw/cw} - \omega_m$).

Lastly, we discuss the experimental controllability for the parameters to realize the threefold symmetry. First, regarding the frequency degeneracy of ccw and cw modes, for the planar microwave ring resonators, such as the microstrip ring, the resonant frequencies for ccw and cw modes with same mode number are highly degenerate, unless the extra geometrical

perturbations are introduced [40,41]. Therefore, the $\omega_{ccw/cw}$ can be regarded as degenerate when the microwave circuit has threefold geometrical symmetry. Next, for the external coupling rates among the ccw and cw modes and three waveguides ($\kappa_{ccw,e1(2,3)}$ and $\kappa_{cw,e1(2,3)}$), as the ccw and cw modes are highly degenerate, the external coupling rate between each waveguide and the ring is determined by the impedance [42–44], which depends on the geometrical dimensions and dielectric substrate material [35,45]. Thus, by utilizing precise lithographical patterning, we can engineer the waveguides on the same chip with identical geometry yielding threefold symmetry. The degeneracy of external coupling rates can be well controlled and modeled at the microwave frequencies. Other literatures also explored tuning external coupling rates dynamically during the measurements by utilizing a superconducting quantum interference device [46]. For the microwave intrinsic dissipation rate κ_i of the superconducting ring, this value is minimal at the cryogenic temperature to be around several megahertz [47], and can be regarded as evenly dissipated to three ports in consideration of the system symmetry.

III. MATERIAL PLATFORMS

In this session, we are interested in implementing circulators via both high-spin-density and low-spin-density ferrimagnetic materials. To achieve circulators with low insertion loss and high isolation, an ideal ferrimagnetic material should have the low Gilbert damping factor ζ . A wide exploited

TABLE I. Material parameters for YIG and V[TCNE]₂.

Name	$4\pi M_s$	Δf @ ~ 10 GHz	Thickness
YIG bulk	1750 G	3 MHz	~ 1 mm
YIG thin film	1750 G	3 MHz	1–5 μ m
V[TCNE] ₂	90 G	2 MHz	1–5 μ m

high-density ferrimagnetic material is the single-crystal ferrimagnetic material yttrium iron garnet (YIG; $\zeta_{\text{YIG}} \sim 3 \times 10^{-5}$) [29,48–52], whereas a particularly interesting low-density ferrimagnetic material is organic-based ferrimagnet vanadium tetracyanoethylene thin films (V[TCNE]₂, $\zeta_{\text{V[TCNE]}_2} \sim 3.8 \times 10^{-5}$) [31,53,54]. The relevant material parameters of bulk and thin-film YIG as well as V[TCNE]₂ are listed in Table I [26,48,53].

A. YIG-based circulator

YIG is widely used as the magnon media for its excellent magnetic properties such as long spin lifetime and wide tunability. YIG has a relatively large saturation magnetization ($4\pi M_s$, 1750 G [55]), which is about 20 times higher than that of V[TCNE]₂, and thus can be regarded as a high-spin-density material [29,31,48–54]. Recently, YIG thin films and spheres have been used to study the coherent coupling between magnons and microwave photons. The reported coupling strengths range from several megahertz to a few gigahertz by engineering the mode overlap factor, mode volume, and resonant frequencies [14,15,15–20,24]. Both YIG thin film and YIG bulk can be promising candidates for building high-performance circulators, due to their low Gilbert damping factors. The key difference is that, for YIG thin film, when magnetized in the out-of-plane direction, the bias field needs to overcome the demagnetization field (~ 1750 Oe) to fully saturate and effectively excite the magnon resonances ($\omega_m = \gamma|\vec{B}_0 - \vec{H}_d|$, where \vec{H}_d is the demagnetizing field). On the other hand, the demagnetization field for the bulk is only around tens of oersted. Thus, compared with bulk, using YIG thin film as the magnon media may introduce extra flux in the superconducting microwave resonator [56,57].

In this session, we show the use of YIG bulk disk as the magnon media to achieve microwave circulation under the condition where the magnon and photon are strongly coupled ($g > \kappa_{\text{ccw}}, \kappa_{\text{cw}}, \kappa_m$), and the superconducting microwave ring resonator is overcoupled ($\kappa_e > \kappa_i$). In this scenario, the magnon resonance can be detuned from the microwave resonance into the dispersive coupling regime to reduce loss induced by ferrimagnetic damping. The inherent tunability of the magnon resonance offers extra functionalities for this system to achieve adjustable isolation ratio and switchable signal propagation directions.

To be compatible with the relatively strong bias magnetic field, superconductors with high critical field, such as the NbTi film on the sapphire substrate, can be used for the microwave circuits fabrication [58]. The proposed device should be designed to maintain the threefold structural symmetry with three identical waveguides inductively coupled with the ring resonator at the $2\pi/3$ angle difference. The resonant frequencies of the ccw and cw modes are determined by

the superconducting resonator geometry, and are degenerate ($\omega_{\text{ccw}} = \omega_{\text{cw}}$) in the absence of the magnon media. The intrinsic microwave loss $\kappa_i/2\pi$ for both microwave modes can be estimated based on the previous literature to be around several megahertz [47,59,60], when the static magnetic field is much lower than the NbTi critical field. The total external coupling rate for the ring resonator can be adjusted by changing the impedance of the input waveguides. Here, based on previous magnon-photon coupling studies within microwave coplanar resonators [19,25], the external coupling rate $\kappa_e/2\pi$ can be engineered from tens of megahertz to several gigahertz. To explore both magnon-photon strong- and weak-coupling regimes, we will set $\kappa_e/2\pi$ to a moderate value (600 MHz), which can be achieved experimentally via the impedance design. Given the system's structural symmetry, the external coupling rates should be identical for both ccw and cw modes.

The magnon-photon coupling strength g can be engineered by changing the microwave mode volume and frequency [33,61], engineering the field overlap [33,34,61], and utilizing materials with different spin densities [33]. During experimental measurements, g can be tuned dynamically by changing the gap between the ferrimagnetic disk and the circuit to effectively tune the field overlap factor [34], adding an additional ground plate to modify the microwave field distribution, and tuning the temperature [62]. Such engineering flexibility offers various techniques for system optimizations.

Figures 2(a) and 2(b) show a mapping of the transmission spectra $|S_{21}|^2$ and $|S_{12}|^2$, respectively, as a function of frequency detunings Δ_m ($\omega_m - \omega_{\text{ccw/cw}}$) and Δ_c ($\omega - \omega_{\text{ccw/cw}}$) calculated from Eqs. (11) and (12), with $g/2\pi = 600$ MHz, $\kappa_e/2\pi = 600$ MHz, $\kappa_i/2\pi = 2$ MHz, and $\kappa_m/2\pi = 3$ MHz. The avoided crossings in the transmission spectra indicate the strong coupling between the microwave photon and the magnon, with clear asymmetric transmission under positive and negative magnon resonance detuning Δ_m . As we can see in the Figs. 2(c) and 2(d), $|S_{21}(-|\Delta_m|)|^2$ equals $|S_{12}(+|\Delta_m|)|^2$. At the same time, the optimal circulation with minimal insertion loss and large isolation ratio ($|\text{iso.}| = 20 \log_{10} |S_{21}|/|S_{12}|$) can be achieved by optimizing the magnon resonance detuning Δ_m . As shown in Figs. 2(c) and 2(d), when $\Delta_m = \pm 0.87$ GHz, the insertion loss (|IL|) can be as low as 0.05 dB, with the isolation ratio reaching 56 dB. Noticeably, the directionality of the signal propagation can be easily switched by changing Δ_m without reorienting the external magnetic field. When the magnon resonance is optimized, the maximal isolation ratio that can be achieved in a system is limited by intrinsic losses κ_i and κ_m . If the system dissipation losses can be optimized to $\kappa_i/2\pi = \kappa_m/2\pi = 0.5$ MHz by the fabrication process optimization and/or operating at ultralow temperatures, the isolation ratio can be further enhanced to 63 dB, with insertion loss being reduced to 0.02 dB.

Next, we study the controllability of the coupled system based on other tuning parameters. Figure 3(a) shows a mapping of the 20 dB isolation bandwidth as a function of the magnon-photon coupling strength g , and the microwave total dissipation rate $\kappa = \kappa_e + \kappa_i$. The degenerate microwave resonant frequency is 10 GHz for this calculation. The contour lines delineate 20, 50, 100, and 200 MHz circulation bandwidths when $|\text{iso.}| = 20$ dB, respectively. The parameter spaces can be divided into four regions. Region I

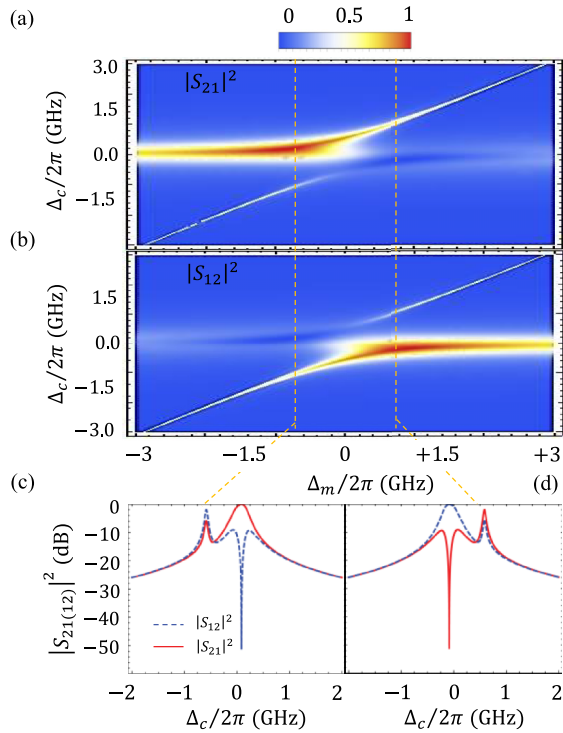


FIG. 2. (a) and (b) are the mapping of the transmission $|S_{21}|^2$ and $|S_{12}|^2$, respectively, as a function of Δ_m and Δ_c , under strongly coupled conditions with $\kappa_e/2\pi = 600$ MHz, $2g/2\pi = 1200$ MHz. The mode splitting at the on-resonance condition is around $2g$. Under different detunings $\Delta_m/2\pi = \pm 0.87$ GHz, the transmission spectra are plotted in (c) [(d)] when YIG is biased with magnetic resonance lower (higher) than the microwave resonance.

represents the weak-coupling regime ($g \ll \kappa$) where the coupling strength is too small to induce significant phase modulation at output ports. Similarly, in region IV, at the ultrastrong-coupling limit when $g \gg \kappa$, the weak signal circulation can be understood as the ccw and cw microwave mode splitting in the frequency domain being much larger than its linewidth, due to the strong coupling with the magnon mode. Thus, the ccw and cw modes have minimal effective overlap in the frequency domain to enable the effective circulation. In region III, when the system is near or at the strong-coupling regime $g \sim \kappa$, the 20 dB isolation bandwidth increases linearly with g and κ . The optimal circulation happens when the magnon mode is detuned away from microwave modes. Lastly, in region II, when the magnon and photon are weakly coupled $g < \kappa$, the isolation bandwidth also yields a linear relation as g and κ are increasing linearly. Compared with region III when the system is near strongly coupled, in region II, the magnon mode is tuned close to the microwave mode to achieve strong enough phase modulation for broadband circulation. These properties show that for different applications, various isolation bandwidths can be engineered by tuning magnon resonant frequency, magnon-photon coupling strength, and microwave total dissipation rate.

Another critical performance parameter of a circulator is the insertion loss ($|\text{IL}|$). In Fig. 3(b), we study the contribution of the microwave intrinsic loss to the insertion loss at different microwave external coupling rates with the

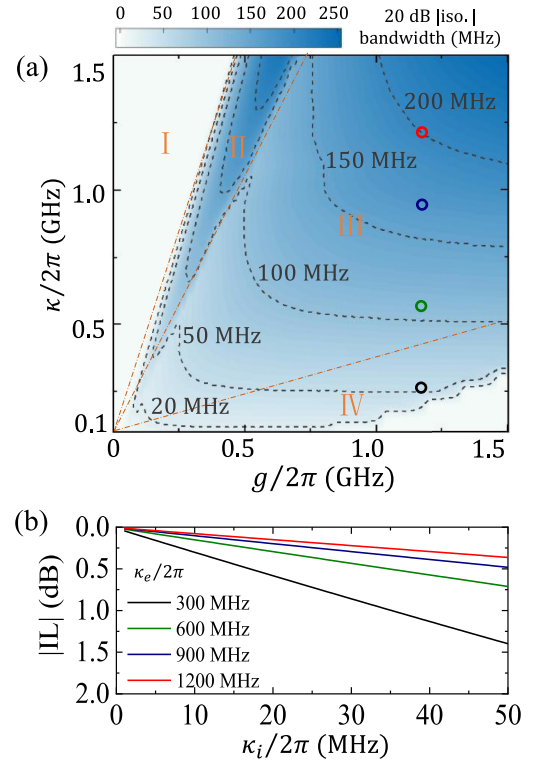


FIG. 3. The 20 dB isolation ratio ($|\text{iso.}|$) bandwidth is plotted in (a) as a function of $g/2\pi$ and $\kappa/2\pi$, where the black dashed lines are contour lines of 20, 50, 100, and 200 MHz $|\text{iso.}|$ bandwidth, respectively. The magnon frequency detuning Δ_m is chosen at each κ and g to maximize the isolation bandwidth. (b) When $g/2\pi$ is set to be 1200 MHz, the insertion loss ($|\text{IL}|$) as a function of $\kappa_i/2\pi$, for different $\kappa_e/2\pi$ is plotted. The colored lines in (b) correspond to the colored circles in (a).

magnon-photon coupling rate fixed at $g/2\pi = 1200$ MHz. As $\kappa_e/2\pi$ is varied from 300 to 1200 MHz, with the increase of κ_i , the $|\text{IL}|$ increases correspondingly. Thus, the high- Q superconducting microwave resonator is ideal for achieving ultralow loss circulation. Figure 3(b) also indicates that at the same microwave intrinsic loss rate κ_i , the insertion loss can be reduced by increasing the microwave external coupling rate κ_e . This is because when κ_e is dominating in the total microwave dissipation rate, less microwave signal in the resonator dissipates into the intrinsic loss channel, thus, resulting in the low insertion loss. The analyses above establish that many desirable features of a circulator—high isolation, low insertion loss, and tunable bandwidth—can be achieved simultaneously.

B. V[TCNE]₂-based circulator

In this session, we focus on the microwave circulation based on the low-spin-density ferrimagnetic material V[TCNE]₂, which is an organic-based high-quality ferrimagnetic semiconductor ($E_g = 0.5$ eV, $\sigma = 0.01$ S/m) exhibiting room temperature magnetic ordering ($T_c > 600$ K) [31,63,64]. V[TCNE]₂ has a very low Gilbert damping factor on a similar level as single-crystal YIG for both continuous and micropatterned films [54]. Particularly, this material can be

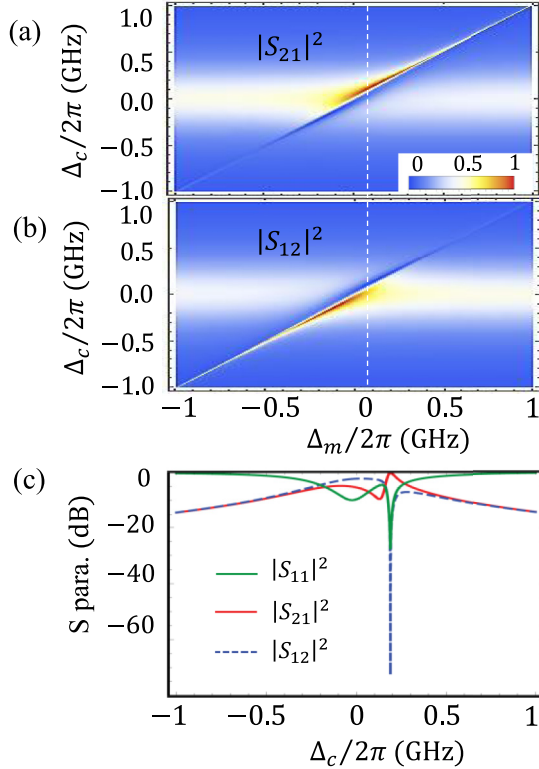


FIG. 4. (a) and (b) are the mappings of the transmission $|S_{21}|^2$ and $|S_{12}|^2$, respectively, as a function of Δ_m and Δ_c . The V[TCNE]₂-based circulator is weakly coupled with $g/2\pi = 100$ MHz and $\kappa_e/2\pi = 600$ MHz. (c) plots the full scattering parameters, showing low |IL| and high |iso.| being achieved simultaneously [corresponding to the bias condition shown by the dashed white line in (a) and (b)].

integrated onto various substrates by chemical vapor deposition while maintaining excellent magnetic properties. Considering high-quality YIG can only be grown on lattice-matched substrates, V[TCNE]₂ can be an alternative solution for highly compact integrated magnonic devices. The saturation magnetization of V[TCNE]₂ (90 G) is over an order of magnitude smaller compared with that of YIG (1750 G), leading to the small demagnetizing field and significantly reduced bias magnetic field which is desired for many applications [57,65,66]. On the other hand, the lower material spin density weakens the magnon-photon coupling strength g under the same microwave circuit design and magnon mode volume, making it difficult to reach strong coupling.

Here, we discuss the microwave circulation when the system is weakly coupled ($\kappa_m < g < \kappa$). For low-spin-density material, we assign the magnon-photon coupling strength $g/2\pi$ to be 100 MHz, with microwave dissipation rates $\kappa_i/2\pi = 2$ MHz, $\kappa_e/2\pi = 600$ MHz, and magnon resonant linewidth $\kappa_m/2\pi = 2$ MHz. The mapping of the transmission scattering parameters is shown in Figs. 4(a) and 4(b). Similar directional transmission between $|S_{12}|^2$ and $|S_{21}|^2$ is observed, with a Lorentzian-shaped transparency window that shows the magnon resonance. A line cut of the transmission map at a fixed bias field, indicated by the white dashed line in Figs. 4(a) and 4(b), is reproduced in Fig. 4(c) as a function of

the excitation frequency. The low insertion loss (0.09 dB) and high isolation ratio (77 dB) can be achieved with optimized detuning ($\Delta_m = 0.16$ GHz). Due to the small magnon-photon coupling strength, the 20 dB isolation bandwidth is around 0.5 MHz, much narrower compared to that of YIG. This narrow-bandwidth circulator nevertheless has promising applications in circuit QED systems where it can serve as the filtering function for multiplexed superconducting qubits and resonators [67–69].

Next, we discuss the circulation performance for the V[TCNE]₂-based narrow-band circulator, when the threefold geometrical symmetry cannot be fully satisfied experimentally. With the same magnon-photon coupling strength, microwave intrinsic dissipation rates, and magnon linewidth, the following two symmetry-breaking conditions are studied. (1) First, the microwave ccw and cw dissipation rates are assigned to be nondegenerate and differ by 20% ($\kappa_{ccw,e}/2\pi = 600$ MHz, $\kappa_{cw,e}/2\pi = 720$ MHz). When the system is biased at the same magnon detuning ($\Delta_m = 0.16$ GHz) compared with the symmetrical device, as shown by the dashed lines in Fig. 5(a), the isolation ratio decreases to 27 dB. However, by optimizing the magnon detuning to 0.21 GHz, the high isolation (61 dB) and low insertion loss (0.16 dB) can be achieved again at a slightly different frequency, indicated by the solid lines in Fig. 5(a). (2) Second, the slight differences among external coupling rates between waveguides to the ring resonator can be introduced experimentally, due to the imperfections during device patterning and packaging. Here, the total external coupling rates for the ccw and cw modes are designed to be the same ($\kappa_{ccw,e} = \kappa_{cw,e} = \kappa_e = 2\pi \times 600$ MHz), while the coupling rates to three waveguides are $\frac{1}{2}\kappa_e$, $\frac{1}{3}\kappa_e$, and $\frac{0.8}{3}\kappa_e$, respectively. When the magnon detuning Δ_m remains the same as the symmetrical case, illustrated by the dashed lines in Fig. 5(b), the isolation ratio decreases drastically to 19 dB. Similarly, the high-performance circulation can be restored via tuning magnon resonances (isolation ratio: 67 dB; insertion loss: 0.15 dB), as shown by the solid lines in Fig. 5(b). It is worth noting that because the system does not maintain the threefold symmetry, leading to $S_{21} \neq S_{13} \neq S_{32}$, the magnon detuning can only be optimized for one type of connections. Despite the potential system imperfections during the experimental implementations, the tunable magnon resonance can optimize the signal interferences at different ports dynamically to achieve high-performance circulation.

Also, in the undercoupled scenario, the magnon resonance needs to be tuned close to the microwave resonance, so the overall insertion loss is more sensitive to the magnon linewidth κ_m than the strongly coupled system. By operating at cryogenic temperatures with reduced $\kappa_m/2\pi = 0.5$ MHz, the |IL| can be further decreased to 0.04 dB for the ideal symmetric device and 0.06 dB for the nonsymmetric device as we discussed above, while maintaining |iso.| > 50 dB.

Recently, a technique for micropatterning of V[TCNE]₂ thin films has been developed for creating high-fidelity lithographically defined structures without observable deterioration of magnetic properties [54]. With further improvement of the magnon-microwave mode overlap and a reduction of the magnon-mode volume, higher magnon-photon coupling strength can be realized even with a low-spin-density

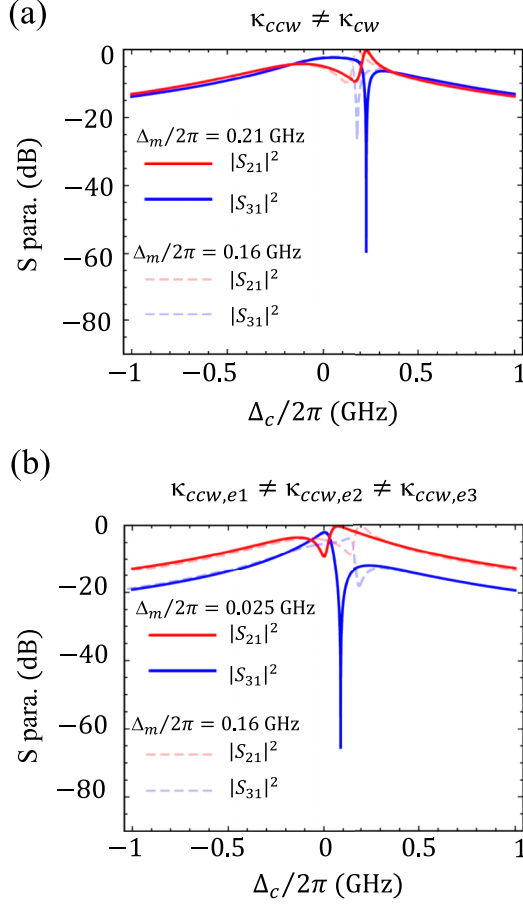


FIG. 5. (a) Transmission spectra of V[TCNE]₂-based circulator when the ccw and cw modes have different total external coupling rates ($\kappa_{ccw,e}/2\pi = 600$ MHz, $\kappa_{cw,e}/2\pi = 720$ MHz). The solid lines are transmission S parameters when the Δ_m is 0.21 GHz, while the dashed lines are the transmission parameters when the magnon detuning remains the same as in the symmetrical V[TCNE]₂ circulator. (b) Transmission spectra when the external coupling rates to each waveguide are nondegenerate. The solid and dashed lines denote the S parameters under the optimized and unoptimized magnon detunings, respectively.

V[TCNE]₂ system, giving rise to a broader operating bandwidth.

IV. CONCLUSION

In summary, we have theoretically investigated a high-performance microwave signal circulation based on a multiport coupled magnon-photon system. The nonreciprocity arises from the interference between the two counterpropagating microwave modes, introduced by the chirality-dependent coupling with the magnon excitation. The device implementations are analyzed using practical parameters of the superconducting microwave circuit and low Gilbert damping factor materials (YIG and V[TCNE]₂). High-performance microwave circulation with low insertion loss (<0.05 dB) and high isolation ratio (>56 dB) can be achieved with both high- and low-spin-density materials. Although the obtainable

isolation bandwidth in the low-spin-density material (V[TCNE]₂) is narrower than the high-spin-density platform (YIG), it is beneficial for applications that desire frequency-selective isolation such as superconducting quantum computing systems, for example, to isolate the qubits from the environment and to curtail Purcell decay [68,69]. Additional advantages of this magnon-photon system include great tunability and directional switchability. The proposed theory is general and can be applied to study multimode-induced nonreciprocity in other hybrid systems, such as the quantum optical circulators based on chiral atom-light coupling [70,71].

ACKNOWLEDGMENTS

We acknowledge funding support from National Science Foundation (EFMA-1741666). H.X.T. acknowledges support from a Packard Fellowship in Science and Engineering.

APPENDIX

1. Proof of $M_2^\dagger M_2 = \Gamma_e$

We denote the external and intrinsic dissipation matrices for the microwave signal as

$$\Gamma_e = \begin{pmatrix} \kappa_{ccw,e} & 0 & 0 \\ 0 & \kappa_{cw,e} & 0 \\ 0 & 0 & 0 \end{pmatrix},$$

and

$$\Gamma_i = \begin{pmatrix} \kappa_{ccw,i} & 0 & 0 \\ 0 & \kappa_{cw,i} & 0 \\ 0 & 0 & \kappa_m \end{pmatrix}.$$

Consider a special case with no incident wave ($s_{in} = 0$) and no intrinsic loss ($\Gamma_i = 0$). Due to energy conservation, the decay of the intracavity energy should equal to the output power $-\frac{d(\mathbf{a}^\dagger \mathbf{a})}{dt} = \mathbf{s}_{out}^\dagger \mathbf{s}_{out}$. From Eq. (3), we have

$$\frac{d(\mathbf{a}^\dagger \mathbf{a})}{dt} = \frac{d\mathbf{a}^\dagger}{dt} \mathbf{a} + \mathbf{a}^\dagger \frac{d\mathbf{a}}{dt} = \mathbf{a}^\dagger (\mathbf{M}_1^\dagger + \mathbf{M}_1) \mathbf{a} = -\mathbf{a}^\dagger \Gamma_e \mathbf{a}. \quad (\text{A1})$$

On the other hand, the output power is

$$\mathbf{s}_{out}^\dagger \mathbf{s}_{out} = \mathbf{a}^\dagger \mathbf{M}_2^\dagger \mathbf{M}_2 \mathbf{a}. \quad (\text{A2})$$

Comparing Eqs. (A1) and (A2) above, we get

$$\mathbf{M}_2^\dagger \mathbf{M}_2 = \Gamma_e. \quad (\text{A3})$$

2. Proof of $-\mathbf{C}^\dagger \mathbf{M}_2 = \mathbf{K}^\dagger$

From energy conservation, we can predict that $\mathbf{s}_{in}^\dagger \mathbf{s}_{in} - \mathbf{s}_{out}^\dagger \mathbf{s}_{out} = \frac{d(\mathbf{a}^\dagger \mathbf{a})}{dt} + \mathbf{a}^\dagger \Gamma_i \mathbf{a}$. Combining Eqs. (3), (4), and (A3), we can have

$$\mathbf{s}_{in}^\dagger \mathbf{C}^\dagger \mathbf{M}_2 \mathbf{a} + \mathbf{a}^\dagger \mathbf{M}_2^\dagger \mathbf{C} \mathbf{s}_{in} = -\mathbf{s}_{in}^\dagger \mathbf{K}^\dagger \mathbf{a} - \mathbf{a}^\dagger \mathbf{K} \mathbf{s}_{in}. \quad (\text{A4})$$

Therefore, we can get $-\mathbf{C}^\dagger \mathbf{M}_2 = \mathbf{K}^\dagger$.

According to the relation among \mathbf{K} , \mathbf{C} , and \mathbf{M}_2 , we can drive the expression of matrix \mathbf{K} as shown in Eq. (6), and the full scattering matrix can be calculated from Eq. (8).

- [1] C. Caloz, A. Alù, S. Tretyakov, D. Sounas, K. Achouri, and Z.-L. Deck-Léger, *Phys. Rev. Appl.* **10**, 047001 (2018).
- [2] D. K. Linkhart, *Microwave Circulator Design* (Artech House Inc., 1989).
- [3] C. Fay and R. Comstock, *IEEE Trans. Microwave Theory Tech.* **13**, 15 (1965).
- [4] Y. Wu and F. J. Rosenbaum, *IEEE Trans. Microwave Theory Tech.* **22**, 849 (1974).
- [5] N. R. Bernier, L. D. Toth, A. Koottandavida, M. A. Ioannou, D. Malz, A. Nunnenkamp, A. Feofanov, and T. Kippenberg, *Nat. Commun.* **8**, 604 (2017).
- [6] G. A. Peterson, F. Lecocq, K. Cicak, R. W. Simmonds, J. Aumentado, and J. D. Teufel, *Phys. Rev. X* **7**, 031001 (2017).
- [7] K. Fang, J. Luo, A. Metelmann, M. H. Matheny, F. Marquardt, A. A. Clerk, and O. Painter, *Nat. Phys.* **13**, 465 (2017).
- [8] A. Metelmann and A. A. Clerk, *Phys. Rev. X* **5**, 021025 (2015).
- [9] B. J. Chapman, E. I. Rosenthal, J. Kerckhoff, B. A. Moores, L. R. Vale, J. A. B. Mates, G. C. Hilton, K. Lalumière, A. Blais, and K. W. Lehnert, *Phys. Rev. X* **7**, 041043 (2017).
- [10] B. J. Chapman, E. I. Rosenthal, and K. W. Lehnert, *Phys. Rev. Appl.* **11**, 044048 (2019).
- [11] D. L. Sounas and A. Alù, *Nat. Photonics* **11**, 774 (2017).
- [12] D. D. Stancil and A. Prabhakar, *Spin Waves* (Springer, New York, 2009).
- [13] Y. Tabuchi, S. Ishino, A. Noguchi, T. Ishikawa, R. Yamazaki, K. Usami, and Y. Nakamura, *Science* **349**, 405 (2015).
- [14] X. Zhang, C.-L. Zou, N. Zhu, F. Marquardt, L. Jiang, and H. X. Tang, *Nat. Commun.* **6**, 8914 (2015).
- [15] X. Zhang, C.-L. Zou, L. Jiang, and H. X. Tang, *Sci. Adv.* **2**, e1501286 (2016).
- [16] T. Liu, X. Zhang, H. X. Tang, and M. E. Flatté, *Phys. Rev. B* **94**, 060405(R) (2016).
- [17] A. Osada, R. Hisatomi, A. Noguchi, Y. Tabuchi, R. Yamazaki, K. Usami, M. Sadgrove, R. Yalla, M. Nomura, and Y. Nakamura, *Phys. Rev. Lett.* **116**, 223601 (2016).
- [18] N. Kostylev, M. Goryachev, and M. E. Tobar, *Appl. Phys. Lett.* **108**, 062402 (2016).
- [19] B. Bhoi, T. Cliff, I. Maksymov, M. Kostylev, R. Aiyar, N. Venkataramani, S. Prasad, and R. Stamps, *J. Appl. Phys.* **116**, 243906 (2014).
- [20] B. Bhoi, B. Kim, J. Kim, Y.-J. Cho, and S.-K. Kim, *Sci. Rep.* **7**, 11930 (2017).
- [21] C. Match, M. Harder, L. Bai, P. Hyde, and C.-M. Hu, *Phys. Rev. B* **99**, 134445 (2019).
- [22] M. Harder, L. Bai, P. Hyde, and C.-M. Hu, *Phys. Rev. B* **95**, 214411 (2017).
- [23] X. Zhang, T. Liu, M. E. Flatté, and H. X. Tang, *Phys. Rev. Lett.* **113**, 037202 (2014).
- [24] Y. Li, T. Polakovic, Y.-L. Wang, J. Xu, S. Lendinez, Z. Zhang, J. Ding, T. Khaire, H. Saglam, R. Divan *et al.*, *Phys. Rev. Lett.* **123**, 107701 (2019).
- [25] Y.-P. Wang, J. W. Rao, Y. Yang, P.-C. Xu, Y. S. Gui, B. M. Yao, J. Q. You, and C.-M. Hu, *Phys. Rev. Lett.* **123**, 127202 (2019).
- [26] X. Zhang, A. Galda, X. Han, D. Jin, and V. M. Vinokur, *Phys. Rev. Appl.* **13**, 044039 (2020).
- [27] A. D. Córcoles, E. Magesan, S. J. Srinivasan, A. W. Cross, M. Steffen, J. M. Gambetta, and J. M. Chow, *Nat. Commun.* **6**, 6979 (2015).
- [28] S. Kono, K. Koshino, Y. Tabuchi, A. Noguchi, and Y. Nakamura, *Nat. Phys.* **14**, 546 (2018).
- [29] M. Sparks, *Ferromagnetic-Relaxation Theory* (McGraw-Hill, New York, 1964).
- [30] Y. Zhang, X. Feng, K. Zhu, X. Yang, and H. Li, in *2016 IEEE International Conference on Microwave and Millimeter Wave Technology (ICMMT)*, Vol. 1 (IEEE, New York, 2016), pp. 425–427.
- [31] H. Yu, M. Harberts, R. Adur, Y. Lu, P. C. Hammel, E. Johnston-Halperin, and A. J. Epstein, *Appl. Phys. Lett.* **105**, 012407 (2014).
- [32] L. R. Walker, *Phys. Rev.* **105**, 390 (1957).
- [33] J. Li, S.-Y. Zhu, and G. S. Agarwal, *Phys. Rev. Lett.* **121**, 203601 (2018).
- [34] X. Zhang, C.-L. Zou, L. Jiang, and H. X. Tang, *Phys. Rev. Lett.* **113**, 156401 (2014).
- [35] D. M. Pozar, *Microwave Engineering* (Wiley, New York, 2009).
- [36] A. Adamyan, S. Kubatkin, and A. Danilov, *Appl. Phys. Lett.* **108**, 172601 (2016).
- [37] F. Caspers, RF engineering basic concepts: S-parameters, [arXiv:1201.2346](https://arxiv.org/abs/1201.2346) (2012).
- [38] D. Bothner, M. Knufinke, H. Hattermann, R. Wölbing, B. Ferdinand, P. Weiss, S. Bernon, J. Fortágh, D. Koelle, and R. Kleiner, *New J. Phys.* **15**, 093024 (2013).
- [39] S. Sierra-Garcia and J.-J. Laurin, *IEEE Trans. Antennas Propag.* **47**, 58 (1999).
- [40] G.-L. Wu, W. Mu, D. Li, and Y.-C. Jiao, *Prog. Electromagn. Res.* **78**, 17 (2008).
- [41] S.-M. Han and Y.-S. Kim, in *Proceedings of the 2002 IEEE Radio and Wireless Conference (Cat. No. 02EX573) (RAWCON 2002)* (IEEE, New York, 2002), pp. 79–82.
- [42] M. Krawczyk, Master's thesis, Technische Universität München, 2011.
- [43] I. Besedin and A. P. Menushenkov, *EPJ Quantum Technol.* **5**, 2 (2018).
- [44] K. Chang and L.-H. Hsieh, *Microwave Ring Circuits and Related Structures* (Wiley, New York, 2004), Vol. 156.
- [45] L. G. Maloratsky, *Microwaves RF* **39**, 79 (2000).
- [46] B. Peropadre, D. Zueco, F. Wulschner, F. Deppe, A. Marx, R. Gross, and J. J. García-Ripoll, *Phys. Rev. B* **87**, 134504 (2013).
- [47] M. Xu, X. Han, W. Fu, C.-L. Zou, M. H. Devoret, and H. X. Tang, *Appl. Phys. Lett.* **114**, 192601 (2019).
- [48] Y. Sun, Y.-Y. Song, H. Chang, M. Kabatek, M. Jantz, W. Schneider, M. Wu, H. Schultheiss, and A. Hoffmann, *Appl. Phys. Lett.* **101**, 152405 (2012).
- [49] N. Zhu, H. Chang, A. Franson, T. Liu, X. Zhang, E. Johnston-Halperin, M. Wu, and H. X. Tang, *Appl. Phys. Lett.* **110**, 252401 (2017).
- [50] H. Chang, P. Li, W. Zhang, T. Liu, A. Hoffmann, L. Deng, and M. Wu, *IEEE Magn. Lett.* **5**, 1 (2014).
- [51] M. Onbasli, A. Kehlberger, D. Kim, G. Jakob, M. Kläui, A. Chumak, B. Hillebrands, and C. Ross, *APL Mater.* **2**, 106102 (2014).
- [52] G. F. Dionne, *Magnetic Oxides* (Springer, New York, 2009), Vol. 14.
- [53] N. Zhu, X. Zhang, I. Froning, M. E. Flatté, E. Johnston-Halperin, and H. X. Tang, *Appl. Phys. Lett.* **109**, 082402 (2016).
- [54] A. Franson, N. Zhu, S. Kurfman, M. Chilcote, D. R. Candido, K. S. Buchanan, M. E. Flatté, H. X. Tang, and E. Johnston-Halperin, *APL Materials* **7**, 121113 (2019).
- [55] M. Wu, *Solid State Physics* (Elsevier, New York, 2010), Vol. 62, pp. 163–224.

- [56] E. H. Brandt, *Phys. Rev. B* **58**, 6506 (1998).
- [57] P.-G. De Gennes, *Superconductivity of Metals and Alloys* (CRC Press, Boca Raton, FL, 2018).
- [58] Y. Shapira and L. Neuringer, *Phys. Rev.* **140**, A1638 (1965).
- [59] R. Barends, J. Baselmans, J. Hovenier, J. Gao, S. Yates, T. Klapwijk, and H. Hoevers, *IEEE Trans. Appl. Supercond.* **17**, 263 (2007).
- [60] M. Ebrahimi, N. Stallkamp, W. Quint, M. Wiesel, M. Vogel, A. Martin, and G. Birkel, *Rev. Sci. Instrum.* **87**, 075110 (2016).
- [61] H. Huebl, C. W. Zollitsch, J. Lotze, F. Hocke, M. Greifenstein, A. Marx, R. Gross, and S. T. B. Goennenwein, *Phys. Rev. Lett.* **111**, 127003 (2013).
- [62] H. Maier-Flaig, M. Harder, S. Klingler, Z. Qiu, E. Saitoh, M. Weiler, S. Geprägs, R. Gross, S. Goennenwein, and H. Huebl, *Appl. Phys. Lett.* **110**, 132401 (2017).
- [63] J. M. Manriquez, G. T. Yee, R. S. McLean, A. J. Epstein, and J. S. Miller, *Science* **252**, 1415 (1991).
- [64] K. I. Pokhodnya, A. J. Epstein, and J. S. Miller, *Adv. Mater.* **12**, 410 (2000).
- [65] J. Osborn, *Phys. Rev.* **67**, 351 (1945).
- [66] A. Rogachev, A. T. Bollinger, and A. Bezryadin, *Phys. Rev. Lett.* **94**, 017004 (2005).
- [67] Y. Ma, S. L. Danilishin, C. Zhao, H. Miao, W. Z. Korth, Y. Chen, R. L. Ward, and D. G. Blair, *Phys. Rev. Lett.* **113**, 151102 (2014).
- [68] P. Krantz, M. Kjaergaard, F. Yan, T. P. Orlando, S. Gustavsson, and W. D. Oliver, *Appl. Phys. Rev.* **6**, 021318 (2019).
- [69] J. Heinsoo, C. K. Andersen, A. Remm, S. Krinner, T. Walter, Y. Salathé, S. Gasparinetti, J.-C. Besse, A. Potočnik, A. Wallraff *et al.*, *Phys. Rev. Appl.* **10**, 034040 (2018).
- [70] M. Scheucher, A. Hilico, E. Will, J. Volz, and A. Rauschenbeutel, *Science* **354**, 1577 (2016).
- [71] P. Lodahl, S. Mahmoodian, S. Stobbe, A. Rauschenbeutel, P. Schneeweiss, J. Volz, H. Pichler, and P. Zoller, *Nature (London)* **541**, 473 (2017).